Environmental Science Nano

ROYAL SOCIETY OF CHEMISTRY

PAPER

View Article Online
View Journal | View Issue

Check for updates

Cite this: *Environ. Sci.: Nano*, 2025, **12**, 502

Interfacial behavior of ceria grown on graphene oxide and its use for hydrolytic and photocatalytic decomposition of bisphenols A, S, and F†

Martin Šťastný,[a] Dmytro Bavol,[a] Jakub Tolasz,[a] Petr Bezdička,[a] Jan Čundrle,[ab] Martin Kormunda,[c] Ivan Dimitrov,[d] Pavel Janoš,[b] Kaplan Kirakci[a] and Jiří Henych*[ab]

Received 29th August 2024,
Accepted 29th October 2024

DOI: 10.1039/d4en00787e

rsc.li/es-nano

Bisphenol A (BPA) and its structural analogues such as bisphenol S (BPS) and F (BPF) are widespread industrial chemicals of great concern in water and other even biological matrices due to their accumulation and toxicological effects including interference with hormones of the human body. In this work, composites based on CeO_2 nanoparticles grown *in situ* on graphene oxide (GO) sheets were prepared by a low-temperature water-based method and used for the removal of bisphenols from water. It has been demonstrated that ceria-based nanomaterials can spontaneously decompose BPS containing a sulfonyl functional group by hydrolytic cleavage upon its adsorption, while BPA and BPF can be efficiently decomposed by simulated solar light using CeO_2/GO composites as photocatalysts, as shown by the following degradation kinetics and mechanism by HPLC-DAD and HPLC-HRMS. In addition, the study of photophysical and other properties showed that in order to achieve significant interfacial interactions, it is advantageous to use methods of *in situ* growth of nanoparticles on suitable counterparts, such as graphene oxide.

Environmental significance

The presence of bisphenol A (BPA) and its structural analogues such as bisphenol S (BPS) and F (BPF) in water exceeds acceptable safety levels, posing a serious health risk to people worldwide. Development of new methods, including the use of nanomaterials for their removal, is therefore highly desirable. This study shows CeO_2 nanocomposites with graphene oxide (GO) as effective tools for the spontaneous hydrolytic cleavage of BPS and the photocatalytic decomposition of BPA and BPF into various products, which were identified by HPLC-HRMS. It has also been shown that synthesis methods using water as the only green solvent and mild temperatures can enable the *in situ* growth of nanoparticles on GO sheets, which is needed to achieve significant interfacial effects.

Introduction

Cerium is a representative of the rare earth elements (REEs), which are also referred to as "industrial vitamins"[1] as they are used in many high-tech applications from electric vehicles amd rechargeable batteries to lasers or magnets. The attractive properties of REEs stem from the nature of the 4f orbitals[2] that in the case of cerium are energetically close to the valence $5d^1$ and $6s^2$ orbitals, which gives cerium a dual valence state and quite unique physicochemical properties among REEs.[3] The most common compound of cerium, cerium dioxide (or ceria), is a reducible oxide[4] with easy formation of oxygen vacancies and high oxygen storage capacity and mobility in a relatively rigid face-centered cubic fluorite lattice.[5] These properties, together with the unique ability to rapidly switch between Ce^{4+}/Ce^{3+} states allow many

[a] *Institute of Inorganic Chemistry of the Czech Academy of Sciences, Materials Chemistry Department, 250 68 Husinec-Řež, Czechia. E-mail: henych@iic.cas.cz*
[b] *Faculty of Environment, Jan Evangelista Purkyně University in Ústí nad Labem, Pasteurova 3632/15, 400 96 Ústí nad Labem, Czechia*
[c] *Faculty of Science, Jan Evangelista Purkyně University in Ústí nad Labem, Pasteurova 3632/15, 400 96 Ústí nad Labem, Czechia*
[d] *Institute of Organic Chemistry with Centre of Phytochemistry, Bulgarian Academy of Sciences, Sofia, 1113, Bulgaria*

† Electronic supplementary information (ESI) available: Contains XRD and HPLC-DAD measurement details; sample extraction procedure; additional SEM and TEM images; zeta potential distribution of aqueous sample dispersions; XPS spectra of selected samples; HPLC chromatograms of selected samples and standards; mass spectra of standards and selected time-resolved samples; BPS degradation kinetics for samples CeGO5 and CeGO10; photocatalytic degradation scheme for BPA and BPF. See DOI: https://doi.org/10.1039/d4en00787e

industrial and even more newly investigated applications of ceria. Although most of them utilize its redox activity, CeO_2 also possess quite exceptional acid/base,[6] optical and electronic properties, which all together may be relevant in very diverse research areas including low-temperature water–gas shift (WGS) reactions,[7] solid oxide fuel cells,[7] sensors, electrochromic thin-films and many others.

Nevertheless, ceria, especially its nanoparticles (CeNPs), receive much attention also in biological, medicinal and environmental applications.[5,8] This mainly includes all kinds of catalytic, electrocatalytic and photocatalytic reactions,[5] for example, CO_2 or NO_x reduction,[9,10] degradation of organic pollutants in water or VOC in the air, hydrogenation and organic synthesis reactions.[11] In the biosciences, CeO_2-based materials are investigated in bioscaffolding[12] and wound-healing,[13] drug delivery or bioanalysis, but perhaps the most studied are their anti- and pro-oxidant and so-called multi-enzyme mimetic properties,[2] as it is hard to find more versatile inorganic materials that show oxidase,[14] peroxidase,[14,15] catalase,[14,16] superoxide dismutase,[16] or phosphatase[17] mimetic activities.

In a series of studies in *Environmental Science: Nano* our team described the dephosphorylation capabilities of prepared and commercial nanoceria on ATP-like substrates[18] and other nucleotides such as nicotine adenine dinucleotide (NAD) or thiamine pyrophosphate (TPP),[19] or more resistant phosphoester bonds in the 3′,5′-cyclic adenosine monophosphate (cAMP),[20] which mimics bonds in nucleic acids. In dephosphorylation of *p*-nitrophenyl phosphorylcholine (*p*-NPPC) and *p*-nitrophenyl thymidine 5′-monophosphate (*p*-NP-TMP) under physiological conditions, we also distinguished the phospholipase C and D-like activity of ceria.[21] Its inherent dephosphorylation activity may be used, for example, for abatement of antibiotic resistance genes (ARGs)[22,23] by dephosphorylation of free (extracellular) DNA/RNA, or for the degradation of organophosphates (OPs) including widely used pesticides (*e.g.*, chlorpyrifos, parathion)[24,25] or infamous chemical warfare agents (CWAs) soman, sarin, or VX.[24,25] It is also worth mentioning that the use of other OP-based compounds such as flame retardants and plasticizes is on the rise.[26,27] Finally, the strong affinity of ceria to phosphorus can be also used to remove/recover both organic and inorganic phosphates from water.[28]

However, the exceptional surface reactivity of ceria goes far beyond dephosphorylation, as shown by a recent DFT study[29] suggesting CeO_2 as a highly potential catalyst for the hydrolysis of amides, amidines, or carboxylates. Based on these theoretical postulates, we experimentally demonstrated the hydrolytic cleavage of sulfonamides,[30] which are the most used veterinary (and human) antibiotics (ATBs) often found in waters where they contribute to the development of ATB resistance. However, ceria can find application in many other acid/base environmentally-oriented catalytic reactions such as dehydration of alcohols, transfer hydrogenation, or other transformations reported in a recent study.[31]

The surface reactivity, photocatalytic activity and other properties of ceria can be further enhanced by creating nanocomposites with, for example, carbon nanomaterials. In particular, graphene oxide (GO) or reduced GO (rGO) are among the most popular as they are cheap, easy to prepare, non-toxic, biocompatible and may bring many benefits, such as improvement of surface area or light absorption and various electronic, synergetic and interfacial effects in the resulting CeO_2/GO or rGO hybrid materials.[32–35] Various strategies were developed for the synthesis of these composites, but hydrothermal synthesis allowing *in situ* growth of ceria nanoparticles on GO/rGO sheets may be the most popular. However, for practical reasons and to increase the scale of the synthesis, it would be desirable to avoid high-pressure autoclave processing, which is difficult or expensive to convert to an industrial scale.

Herein, CeO_2 nanoparticles prepared with a low-temperature (<100 °C) water-based autoclave-free precipitation method were grown *in situ* on GO sheets to obtain CeO_2/GO hybrid materials with enhanced adsorption properties and exceptional surface reactivity and photocatalytic activity towards bisphenols. It was demonstrated for the first that the ceria-based nanomaterials are able to spontaneously decompose endocrine disruptor bisphenol S (BPS) under ambient conditions. Moreover, enhanced solar-induced photodecomposition of bisphenols A (BPA), S (BPS), and F (BPF) was achieved on CeO_2/GO hybrids thanks to the strong interaction and interfacial behavior that was studied by photoluminescence and other methods.

Materials and methods

Sample synthesis

Pure nanoceria and ceria grown on graphene oxide (GO) were prepared by precipitating cerium(III) nitrate hexahydrate aqueous solution with sodium hydroxide followed by treatment with H_2O_2 and refluxing at water boiling temperature for 24 hours as described elsewhere.[30] For CeO_2/GO composites, a a certain amount of home-made GO[36] water suspension (1 mg mL^{-1}) was dispersed in the reaction mixture by ultrasonic treatment to obtain 5, 10, and 20 wt% of GO in the sample denoted accordingly as CeGO5, CeGO10, and CeGO20. Advantageously, this method uses only water as the sole green solvent, which is also perfectly suitable for using water-dispersible GO, and does not utilize an autoclave, high temperature (>100 °C) or calcination. The resulting sample suspensions were thoroughly washed with deionized water using a dialysis membrane and dried by lyophilization.

Characterization methods

A PANalytical X'pert PRO diffractometer with symmetrical Bragg–Brentano configuration with CuKα radiation ($<\lambda>$ = 1.5418 Å) was used to obtain X-ray diffractograms of powder samples. Rietveld refinement was used for calculation of the crystallite size, lattice constant and microstrain. See further details in the (ESI†). An X-ray photoelectron spectroscopy (XPS) apparatus consisting of a SPECS PHOIBOS 100 hemispherical analyzer with a 5-channel detector and a SPECS XR50 achromatic X-ray source equipped with an Al

anode was used to analyze the chemical states of the elements. The XPS data were processed in CasaXPS software. A DXR Raman confocal microscope (Thermo Fisher Scientific) equipped with a 532 nm excitation laser and a Thermo Nicolet NEXUS 670 FTIR spectrometer equipped with an MCT detector were employed to collect Raman and DRIFTS spectra (obtained by accumulating 64 scans with a resolution of 4 cm^{-1}), respectively. Morphology and composition of the samples was studied by scanning (SEM) and transmission electron microscopy (TEM) using an FEI Nova NanoSEM 450 with CBS detector and FEI Talos F200X microscopes (both Thermo Fisher Scientific) with TEM/EDS elemental mapping. The zeta potential of dispersions of the samples in deionized water (pH ~ 6, 0.1 mg mL^{-1}) was determined by electrophoretic light scattering (ELS) on a particle size analyzer Zetasizer Nano ZS (Malvern, UK). Absorption spectra of these aqueous dispersions were recorded using a Quantaurus QY C11347-1 spectrometer equipped with an integration sphere (Hamamatsu, Japan). Luminescence properties were measured on an FLS1000 spectrometer (Edinburgh Instruments, UK) using a cooled PMT-900 photon detection module (Edinburgh Instruments, UK). The FLS1000 spectrometer was also used for time-resolved phosphorescence measurements (λ_{exc} = 340 nm, EPLED Series, λ_{exc} = 405 nm, EPL Series) and the recorded decay curves were fitted to exponential functions with the Fluoracle software (v. 2.13.2, Edinburgh Instruments, UK).

Reactive adsorption and photodegradation tests

The kinetics of (reactive) adsorption and simulated solar light-induced photodegradation of bisphenol A, S, and F were monitored by analytical procedures developed previously[21,30] for measuring ceria-catalyzed reactions. Concretely, 25 mg of powder sample was dispersed by bath sonication (10 min) in 99.5 mL of distilled water in a reagent vial. The vial was covered by aluminum foil to prevent light, and 0.5 mL of stock solution of BPS was added so that the concentration of BPS in the vial was 10 mg L^{-1}. The vial was placed on a shaker (at 560 rpm, 23 ± 1 °C) and at selected times, 1 mL of suspension was sampled into an Eppendorf tube and centrifuged and the supernatants were analyzed by HPLC-DAD. For the photocatalytic tests, a solar light simulator (300 W Xenon short arc lamp, output intensity ~1 SUN, LOT Quantum Design) equipped with fiber optics, AM 1.5G filter, and 35 mm water filter to avoid heating of the sample was used. Briefly, a 10 mm UV-vis quartz cuvette containing 0.875 mg of the powder sample and 3.5 mL of BPS, BPA, or BPF solution (10 mg L^{-1}) was kept under constant stirring for 30 min in the dark with subsequent irradiation by the solar simulator for 210 min. At selected times, 100 μL aliquots were sampled into Eppendorf tubes and centrifuged (18 000 rpm, 30 sec), 900 μL of water was added and the sample was analyzed immediately on an HPLC/DAD system Ultimate 3000 (Thermo Scientific). All photocatalytic tests were performed in duplicate and the average experimental points were plotted with a standard deviation being less than 7% for all experimental points. Blank tests performed without the catalyst confirmed that solar illumination of the BPA, BPS and BPF solution did not lead to any significant decrease in the initial bisphenol concentration in the time frame of the tests performed. See measurement details in the ESI.†

HPLC-HRMS analysis

A Vanquish Core HPLC system equipped with a diode array detector (DAD) and further connected to an Orbitrap Exploris™ 120 mass spectrometer were used to separate and identify the newly formed degradation products from photodegradation of BPA and BPF. The chromatographic conditions were as follows: accucore PFP column (2.6 μm, 150 × 4.6 mm I.D.) at 30 °C; gradient elution with ACN/H_2O (0.1% HCOOH, HPLC gradient grade, Aldrich) from 30/70 (0 min) linearly to 95/5 (11 min), hold at 95/5 ratio (1 min) and then linearly back to 30/70 (in 30 sec) for the equilibration (2.5 min); flow rate, 0.7 mL min^{-1}; detection, DAD (190–800 nm). Samples of the standard were dissolved in H_2O to a final concentration of 10.0 mg L^{-1}. The injection volume of all samples was 20 μL.

High-resolution mass spectrometry (HRMS) measurements were performed with a HESI probe (heated electrospray ionization) in negative mode using nitrogen (4.8 Air Products) as a collision gas. By comparison, the experimental isotopic distribution in the plot of the peaks in the measured spectra corresponded fully to the calculated spectral pattern. The conditions used for the ESI interface: vaporizer temperature 60 °C; N_2 (isolated from air in Genius XE35, Peak Scientific) as a nebulizing sheath gas and auxiliary gas, flow 60 arb. and 15 arb., respectively; spray voltage 3 kV; ion transfer tube temperature 320 °C; RF lens 20% and mass range from 50 to 600.

Results and discussion

Microstructure and ceria growth mechanism on GO

Precipitation of aqueous cerium nitrate solution with sodium hydroxide followed by treatment with hydrogen peroxide and refluxing yields very small (<5 nm) but highly crystalline aggregated ceria nanoparticles as shown by XRD (Fig. 1a, Table 1), Raman spectroscopy (Fig. 1b) and electron microscopy (Fig. 2 and 3, S1 and S2 in the ESI†). The use of water-based synthesis is very convenient for direct and easy use of graphene oxide (GO) with excellent dispersibility in water to create very homogeneous CeO_2/GO nanocomposites. Therefore, it is easy to control the formation of the nanoceria layer covering the sheets of GO. By this process, three CeO_2/GO composites with 5, 10, and 20 wt% of GO were prepared.

Despite the relatively high amount of GO in the samples, XRD (Fig. 1a) showed only diffraction lines of CeO_2 (ICDD card 00-034-0394) in all composites. This may be due to the formation of a ceria cover layer (consistent with the microscopic investigation discussed further below) and the fact that carbon (*i.e.*, GO) also has significantly less

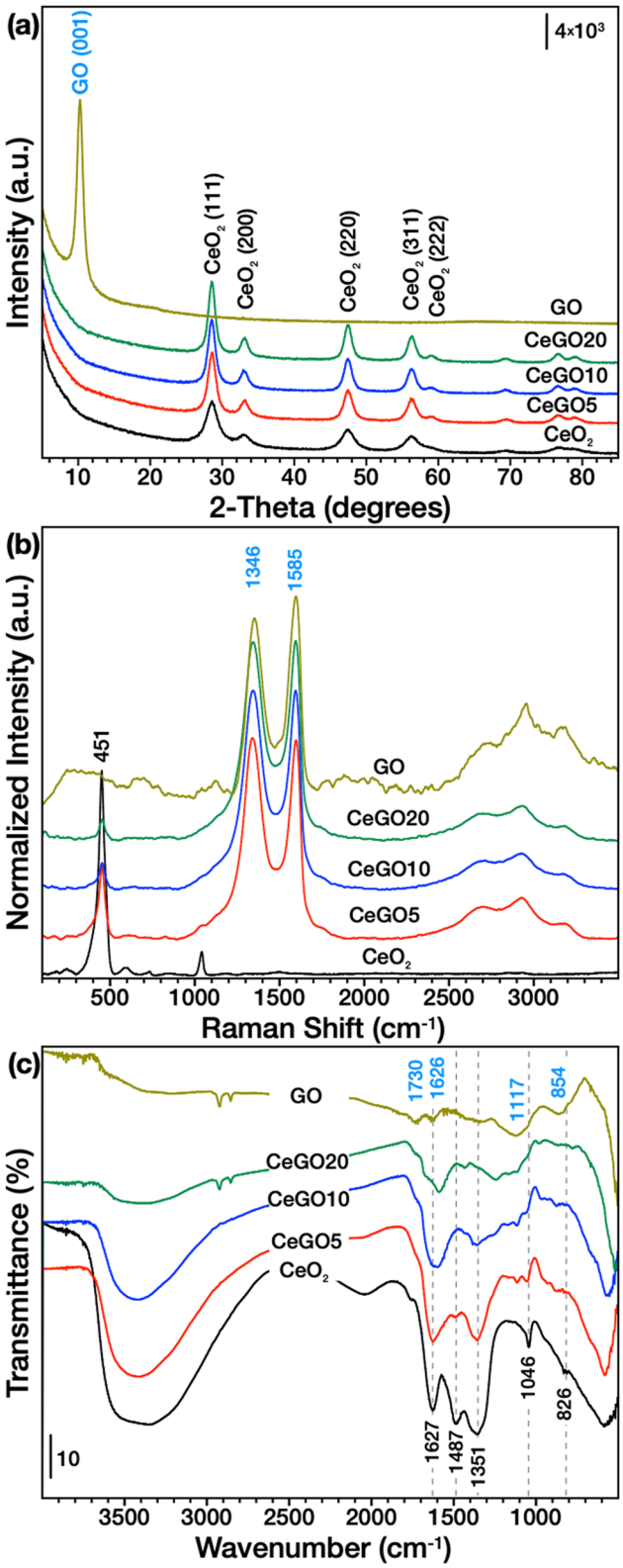

Fig. 1 (a) XRD patterns, (b) Raman spectra and (c) FTIR spectra of CeO_2, GO and their composites.

microabsorption compared to cerium. Moreover, the peak intensity significantly decreases with higher GO dispersion and when the number of adjacent layers decreases, showing the breakdown of the long-range-order stacking,[37] which may be the case for composites in which ceria nanoparticles are grown on the surfaces of GO. However, refluxing GO in the reaction mixture can also cause the formation of defects (*e.g.* by removing oxygenated functionalities), which would also result in a decrease in the diffraction line intensity. Importantly, adding GO in the reaction mixture had a great effect on the crystallization process. As evident in Table 1, the increasing amount of GO leads to a gradual increase in the crystallite size, as calculated by Rietveld refinement, and a decrease in both the lattice constant and the microstrain. The growth in size of nanoceria particles deposited on GO or reduced GO (rGO) has been observed previously[38,39] and was also accompanied by a decrease in surface area (Table 1).

SEM analysis of pure GO showed a typical porous structure of GO sponge[40] formed upon freeze drying of GO aqueous solution. In the composites with high GO concentration (CeGO20, Fig. 2b) ceria forms lone islets and highly dispersed particles on GO sheets. Decreasing GO concentration resulted in forming a continuous thin layer of ceria nanoparticles (CeGO10, Fig. 2c) to full coverage of GO creating a ceria/GO sponge-like porous structure at low GO dosage (CeGO5, Fig. 2d). See more details in higher-magnification SEM images in Fig. S1 in the ESI.† Further investigation was performed by HRTEM (Fig. 3 and S2†). While pure ceria forms dense aggregates of small nanoparticles (<5 nm) with limited interparticle porosity (Fig. S2a,† Table 1), in the composites (Fig. S2b and c†) the ceria nanoparticles are much more dispersed on GO sheets. The particles are also visibly larger compared to pure ceria (consistently with XRD) and importantly, less aggregated exposing various surfaces. Fully exposed individual CeO_2 nanoparticles can be recognized in the CeGO20 sample, which proves that by further increasing the GO concentration, the formation of non-aggregated cerium nanoparticles stabilized on GO sheets can be achieved.

This is likely related to the mechanism of nucleation and growth of the ceria particles in the solution. When GO is dispersed in the reaction mixture, ceria can preferentially nucleate on GO sheets containing various oxygen surface groups. Zeta potential measurements support this assumption (Table 1, Fig. S3†). While pure ceria nanoparticles dispersed in deionized water (pH~6) showed a positive zeta potential of +36 ± 8 mV likely due to the presence of oxygen vacancies, GO exhibited a highly negative potential of −40 ± 8 mV, attributable to its acidic functional groups (OH and COOH). At high pH used for the reaction, GO functional groups are deprotonated and able to bind $Ce^{4+/3+}$ cations, thus providing suitable centers for the preferential nucleation of ceria nanoparticles. Because these centers are spatially separated, at low Ce salt concentration, the ceria nanoparticles are less aggregated (see detailed TEM of CeGO20 in Fig. S2c†) and have enough space to grow larger (see XRD and TEM analysis). The CeGO nanocomposites displayed the expected trend, with the zeta potential decreasing from +29 ± 10 mV to +12 ± 7 mV as the GO mass percentage increased from 5% to 20%, thus reflecting the proportion of acidic functional groups of GO relative to

Table 1 Basic material characteristics obtained from XRD, nitrogen physisorption, Raman spectroscopy and ELS

Sample	Mean crystallite size (XRD), nm	Lattice constant (a), Å	Microstrain (ε)	SA (BET), $m^2\ g^{-1}$	Pore volume, $cm^3\ g^{-1}$	Mean pore diameter, nm	I_D/I_G	ζ-Potential (pH ~ 6), mV
CeO_2	4.1	5.4248	0.0059	219.5	0.19	3.5	—	+36 ± 8
CeGO5	6.8	5.4215	0.0054	190.6	0.27	5.7	1.01	+29 ± 10
CeGO10	7.5	5.4215	0.0047	172.1	0.28	6.5	1.00	+24 ± 8
CeGO20	8.1	5.4214	0.0042	158.6	0.30	7.6	0.99	+12 ± 7
GO	—	—	—	94.0	0.19	7.9	0.90	−40 ± 8

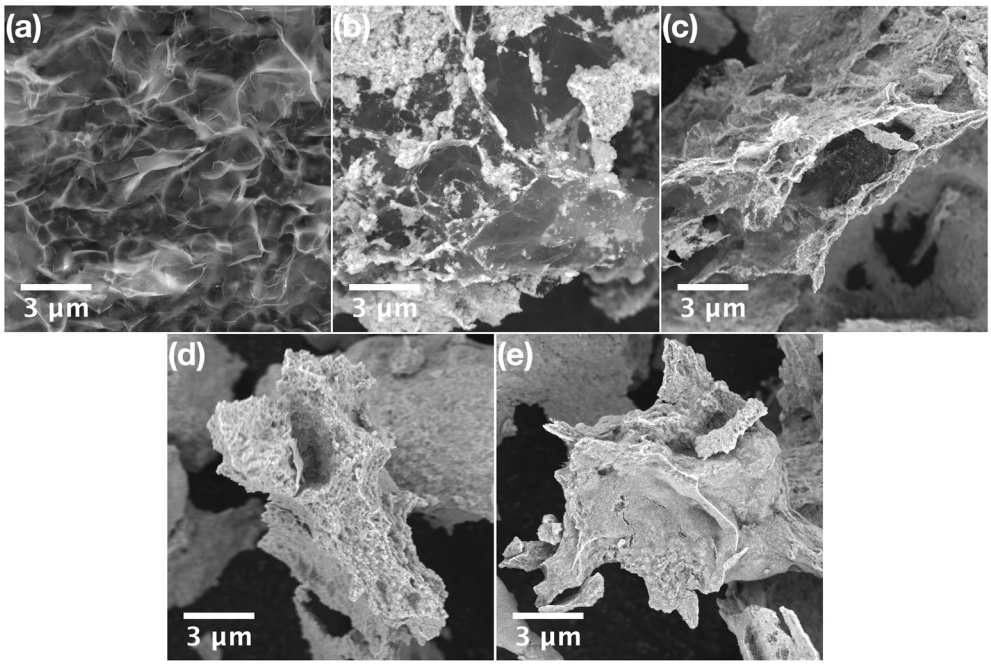

Fig. 2 SEM-CBS images of (a) GO, (b) CeGO20, (c) CeGO10, (d) CeGO05, and (e) pure CeO_2.

positively charged metal centers at the surface of ceria nanoparticles.

Also, the strong electrostatic interaction between ceria and GO may facilitate significant interfacial behavior. This can affect both the reduction rate of GO and the oxidation states of ceria nanoparticles with the easily switchable Ce^{4+}/Ce^{3+} redox couple. Ceria prepared with the hydrogen peroxide-assisted route contains a significant number of defects and reduced states as elaborated previously.[21] However, when GO is added to the reaction solution, it can undergo reduction due to its close contact with nucleating ceria nanoparticles with simultaneous oxidation of Ce^{3+} to Ce^{4+}. This could also explain the decreasing lattice constant and microstrain in ceria particles grown on GO compared to pure CeO_2 (Table 1), as a higher number of reduced states and defects (in pure CeO_2) usually causes higher strain and an increase in unit cell volume in ceria.[41]

XPS analysis (Fig. S4†) further supports the assumption that GO is being reduced in CeGO composites. Compared to pure GO, in the CeGO20 sample, the signal belonging to C═O was reduced while the C–C sp^2 signal was promoted (Fig. S4a†). GO was deconvoluted to individual components according to the literature.[42] The Ce 3d spectra in CeO_2 are in general complex,[20,21,24] showing several interfering peaks (Fig. S4b†). However, in the case of the CeGO20 sample, it seems that two overlapping signals of CeO_2 phases are present, making their proper deconvolution into individual components impossible. Although not entirely clear, these two signals were tentatively assigned to two types of CeO_2 particles in the sample: i) nanoparticles grown directly on GO sheets that interact strongly with GO, and ii) particles that are not in direct contact with GO, but are grown on top of each other in a thicker layer. This is also supported by the analysis of the O 1s region (see Fig. S4c†); just note that due to the complexity the components related to GO are neglected in the spectra of the sample CeGO20.

Analysis by vibrational spectroscopies

Raman spectra (Fig. 1b) showed typical vibration lines of ceria (F_{2g} at ~464 cm^{-1})[43] and GO (D and G bands at ~1346 and ~1585 cm^{-1}, respectively)[44] confirming both phases in the composites but the spectra can also provide some important structural information of the both components.

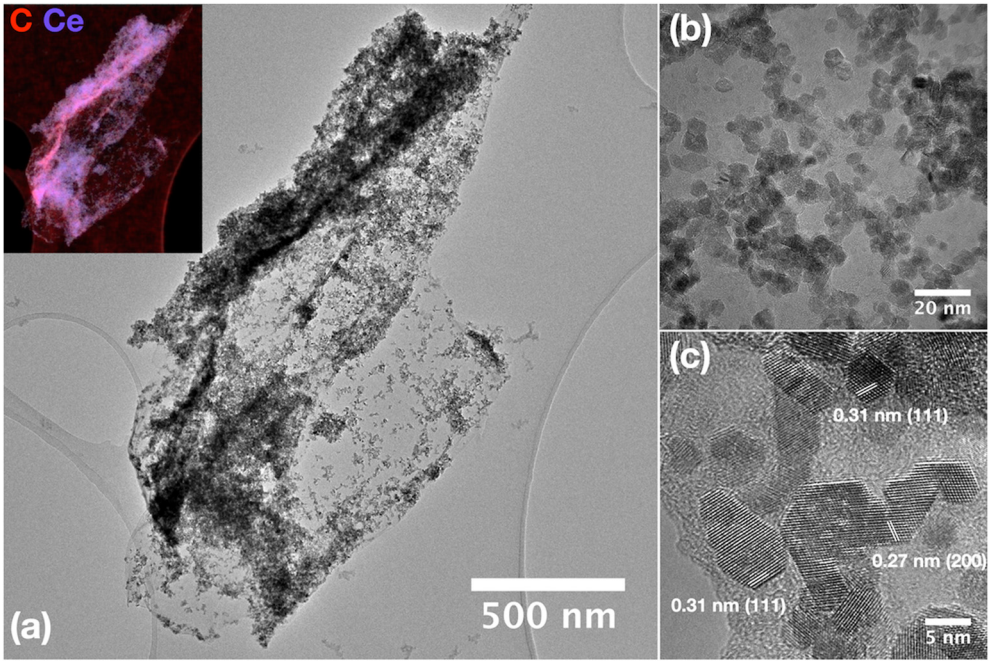

Fig. 3 (a–c) HRTEM images of CeO_2 nanoparticles grown on a GO sheet (CeGO10 sample) with EDS elemental mapping (inset).

For example, the ceria band at ~600 cm^{-1} is related to the structural defects, *i.e.*, oxygen vacancies. This band is clearly visible in pure ceria, but it has practically disappeared in CeGO composites, which may indicate fewer defects as a result of ceria getting oxidized by GO, but it also can be due to a general decrease in the intensity of all ceria vibrations in composites. Although the structure of D and G bands is quite complex,[44] their intensity ratio (I_D/I_G) can be used to estimate the number of defects,[44,45] which is also related to the perturbance of surface oxygen-containing groups. The D band is related to the A_{1g} breathing mode and its intensity is correlated with the number of defects, *i.e.*, it is increasing as a result of reduction.[44,46] The removal of oxygen bonds results in the formation of defects in the graphitic layer, which is not fully compensated by its reconstruction. Thus, the observed increase of the I_D/I_G ratio (see Table 1) of CeGO composites (0.99–1.01) compared to GO (0.90) supports the assumption that GO is being reduced when ceria nanoparticles are grown on its surface.

FTIR spectra of GO (Fig. 1c) show typical vibrations of OH groups at ~3450 cm^{-1}, C=O in carboxylic acid and carbonyl moieties at 1730 cm^{-1}, C=C of skeletal vibrations of graphitic domains combined with the deformation vibration of water at ~1626 cm^{-1}, C–O bonds or epoxy or alkoxy groups forming broad combinatory band centered at ~1117 cm^{-1}, and C–O–C bending motion ~850 cm^{-1}.[47–49] Pure ceria, on the other hand, exhibits strong bands of OH groups and water at ~3450 cm^{-1} and 1627 cm^{-1} as its synthesis proceeds in water without any annealing. Several interfering bands between 1600–1300 cm^{-1} that form upon dissociative adsorption of CO_2 belong to variously coordinated carbonates and carboxylates[50] and also indicate high surface reactivity of the prepared nanoceria. The band at 1046 cm^{-1} (which is also visible in the Raman spectra) is due to the residual nitrates from the starting Ce precursor and the vibration band at 826 cm^{-1} likely belongs to some kind of surface cerium-peroxo species formed upon H_2O_2 treatment during synthesis. The spectra of the composites exhibit combinatory bands of both GO and CeO_2, making proper assignment impossible. However, some important changes in the spectra should be highlighted. Upon GO addition, some bands radically lose their intensity (for example bands at 1487 and 1351 cm^{-1}), while some bands in this region were shifted suggesting significant rearrangement of surface carboxylates and carbonates in nanoceria. Also, new bands that are not visible in bare CeO_2 (or GO) appeared between 1200–1050 cm^{-1} and can indicate perturbance of surface epoxy and alkoxy groups of GO. These spectral changes suggest again the strong interaction between GO and the *in situ* grown CeO_2 nanoparticles.

Photophysical properties

The photophysical properties of the nanocomposites and their individual components were studied in deionized water to assess the extent of their mutual electronic interactions. The normalized absorption and emission spectra are presented in Fig. 4. GO exhibited a featureless absorption profile that gradually decayed in the visible region, with an onset in the NIR. In contrast, CeO_2 showed a sharp absorption band in the UV-A region, peaking at 327 nm. The CeGO20 nanocomposite displayed a UV-A absorption band with a maximum at 309 nm, likely attributable to CeO_2, along with an extended absorption in the visible-NIR region

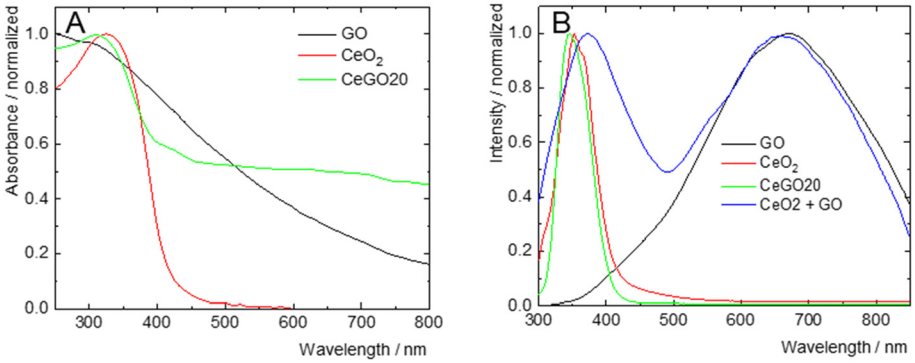

Fig. 4 (A) Normalized absorption spectra of water dispersions of GO, CeO_2, and CeGO20. (B) Normalized luminescence spectra of water dispersions of GO, CeO_2, CeGO20, and the physical mixture of CeO_2 and GO, excitation at 250 nm.

reminiscent of reduced graphene oxide, suggesting the reduction of graphene oxide during the nanocomposite's preparation[51] (Fig. 4A).

Upon excitation at 250 nm, GO exhibited a weak and broad emission spectrum (Fig. 4B), spanning from the UV to the NIR regions, with a maximum at 670 nm and a lifetime of 0.7 ns, characteristic of radiative charge recombination in this material[52] (Fig. 5A). CeO_2, on the other hand, displayed a sharp emission band in the UV-A region with a maximum at 353 nm (Fig. 4B), likely originating from exciton charge recombination, with a very short lifetime (<0.5 ns), below the detection limit of our apparatus (Fig. 5B). The representative nanocomposite (CeGO20) exhibited similar luminescence properties to CeO_2, with a sharp UV-A emission band peaking at 346 nm. Notably, the physical mixture of CeO_2 and GO in the same proportions as CeGO20, which formed the composites by electrostatic interaction (considering their strongly positive and negative zeta potential), retained the emissions of both components (Fig. 4B). The absence of GO emission in CeGO20 may be thus attributed to the reduced state of GO or possibly to photoinduced electron transfer from GO to *in situ* grown CeO_2 nanoparticles. This process would bypass radiative charge recombination in GO and could potentially enhance ROS formation by CeO_2. This hypothesis aligns with the observed increase in the photocatalytic activity of the nanocomposite compared to its individual components (see below).

Reactive adsorption of BPS

The reactivity of nanoceria towards various chemical compounds including a large group of organophosphates (which comprises widespread pesticides, flame retardants, plasticizers, nerve agents, but also biomolecules such as DNA or ATP) is now well known.[5,25,53] However, theoretical work[29] and our recent study[30] indicate that this reactivity may also be relevant for other groups of substances containing ester or other bonds, *e.g.*, sulfonamides. Therefore, we investigated here whether this extraordinary ability could lead to the spontaneous degradation of the endocrine disruptor BPS, which contains a sulfonyl group in its molecule.

When the kinetics of adsorption of BPS from an aqueous solution onto CeO_2 in the dark was monitored, we observed that nanoceria readily adsorbed BPS on its surface (Fig. 6a). To determine whether dissociative adsorption of BPS occurs with concomitant formation of some degradation products, selected time-resolved samples were extracted three times with a 1:1 acetonitrile:water solution (see detailed extraction process in the ESI† and in ref. 30) and analyzed by HPLC/DAD. The formation of two unknown degradation products over time was

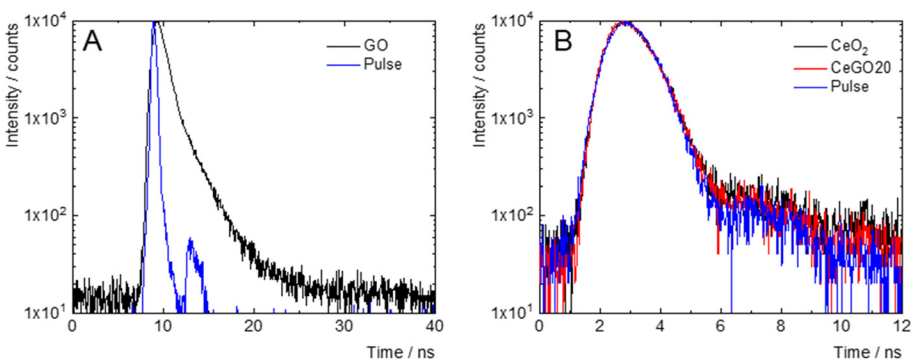

Fig. 5 (A) Fluorescence decay kinetics of aqueous dispersions of GO excited at 405 nm and recorded at 680 nm. (B) Fluorescence decay kinetics of aqueous dispersions of CeO_2 and CeGO20 excited at 340 nm and recorded at 370 nm.

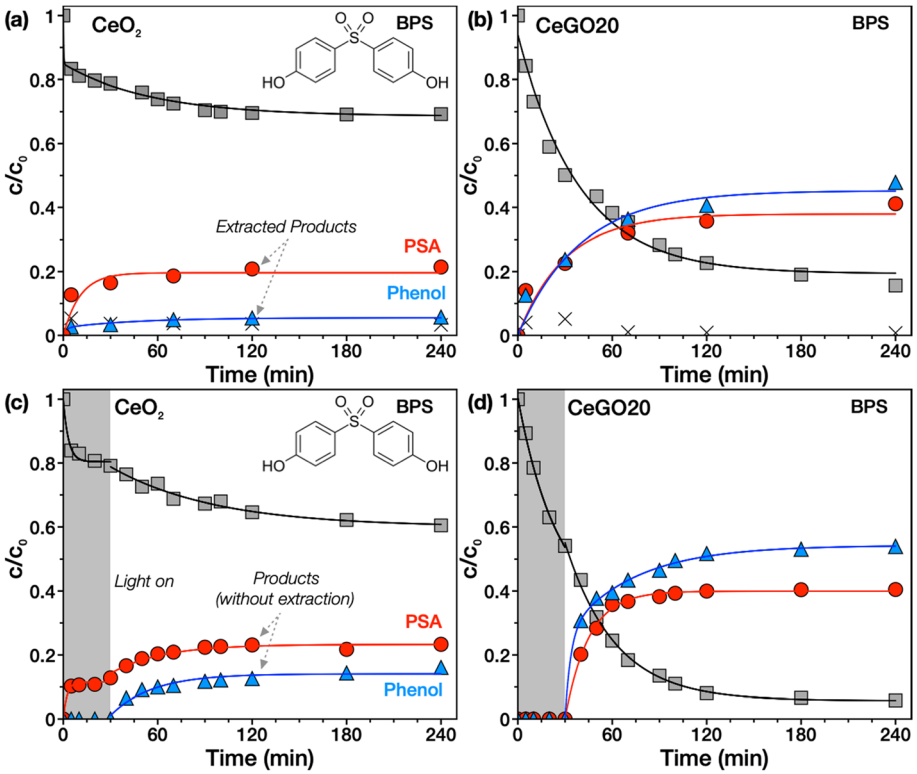

Fig. 6 Reactive adsorption of BPS on (a) CeO_2 and (b) CeO_2 nanoparticles grown on GO (representative sample CeGO20); solar-light enhanced photodecomposition of BPS on (c) CeO_2 and (d) sample CeGO20. Color coding: black squares – BPS concentration in solution, black crosses – BPS extracted from the surface of the catalyst, red circles – PSA and blue triangles – phenol (both extracted in the case of dark tests or released and analyzed directly in solution in photocatalytic tests).

detected in chromatograms (see a representative chromatogram at 120 min in Fig. S4†). These products were identified as phenol (plotted in Fig. 6 as blue triangles) and *p*-phenolsulfonic acid (PSA, red circles) by comparing the retention times of the unknown peaks with standards (Fig. S5†). This indicates that compounds containing a sulfonyl or similar functional group, such as BPS (or previously studied sulfonamide antibiotics[30]), are susceptible to ceria-catalyzed hydrolysis without any illumination, activation or pH adjustment.

Interestingly, all CeGO composites (Fig. 6b, and S6†) showed increased degradation activity compared to pure ceria, while GO alone did not show any degradation of BPS at all (data not shown). The increased degradation rate may be related to the improved availability of the ceria surface due to preventing particle aggregation and possibly also by the contribution of new adsorption sites on the GO sheets. Similar tests were also performed with bisphenols A and F, but no degradation activity was observed, suggesting that only specific functional groups (*e.g.*, ester or sulfonyl) are willing to undergo hydrolysis, as suggested in a recent DFT study.[29]

Photocatalytic decomposition of BPS

Since CeO_2/GO can potentially also be an efficient photocatalyst, the tests were repeated with simulated solar light illumination from 30 min onwards up to 240 min (Fig. 6c and d). In the case of bare CeO_2, only a slight enhancement in BPS degradation was achieved. However, significantly improved desorption of the degradation products (which were identical to those in the no-illumination tests) into the solution could be observed, and therefore it was not necessary to extract the samples. Interestingly, light illumination is likely to stimulate photodesorption of the products that may facilitate catalyst regeneration. This phenomenon was previously observed on TiO_2 in both aqueous media in the case of organic matter[54] or the gas phase for CO.[55] The mechanism is currently unknown but may be related to the photogeneration of charge carriers and recombination of ROS involving oxygen defects.[55]

The light-induced acceleration of the degradation reaction is slightly higher for composites (see the selected representative sample CeGO20, Fig. 6d). In the dark (in the first 30 min), no products are detected in the solution because they are probably adsorbed on the catalyst surface. Note the difference from the assay in Fig. 6b, in which the formed products were desorbed by sample extraction, while in Fig. 6d only the product concentrations in solution are plotted. As can be seen, during the first 30 min (Fig. 6d), the products are not released into the solution, but are adsorbed on the catalyst surface. Interestingly, when illumination was initiated, there was significant photodesorption of the products into solution. This could be significant from a practical point of view – products formed by

reactive adsorption can be retained on the surface of the adsorbent and desorption can be controlled by illumination. Interestingly, reactive adsorption and photocatalytic decomposition of BPS yields the same products in the first stage and may compete with each other. Solar illumination probably only accelerates the desorption of the products and thus the overall reaction rate.

It is evident from the kinetic curves that the amounts of the products (even after extracting the samples, Fig. 6b) are not completely equivalent to the removed bisphenol. We attribute this to an imperfect extraction process and strong binding of products on the surface, or to the fact that other products (*e.g.*, smaller molecules or more polar ones) may be formed that were not identified in our analytical setup.

Photocatalytic decomposition of BPA and BPF

Unlike BPS, which contains a sulfonyl group, BPA and BPF lack functional groups that could be easily hydrolyzed and no hydrolysis products were detected upon adsorption on nanoceria as verified by analyzing the extracts of the reaction suspensions in the dark (data not shown). However, they can be very efficiently photodegraded on the prepared materials (Fig. 7). In the case of BPA (Fig. 7a), pure ceria adsorbed ~20% of its initial amount from the solution in 30 minutes, while with subsequent illumination, only another 19% was removed after 210 min. In contrast, all CeGO nanocomposites showed substantially enhanced photodegradation exceeding 90% BPA removal, while exhibiting similar adsorption of BPA in the dark (between 8–25% BPA removed).

Interestingly, all prepared samples showed significant adsorption of BPF in the dark (Fig. 7c). In particular, the sample CeGO5 removed more than 50% of its initial concentration. The different adsorption behavior of the samples to BPA, BPS, and BPF is likely related to their different polarity. When the reaction solution was irradiated, BPF was degraded even faster than BPA.

Overall, the most efficient sample (CeGO20) removed 100% of BPF, >95% of BPA and ~77% of BPS in 120 min. The different activities of CeGO samples towards bisphenols are likely caused by the different hydrophobicity of bisphenols, which strongly affect their adsorption to the composites. GO (and its partly reduced form) may significantly change the adsorption properties of pure ceria, but more importantly, the interfacial behavior of *in situ* grown CeO_2 on GO, which possibly includes charge transfer between the constituents, seems to be the most relevant for improving the degradation rate.

It may be somewhat surprising that the combination of reactive adsorption and photocatalytic decomposition (in the case of BPS) does not lead to the highest degradation rate. This can be caused by the fact that these phenomena compete with each other or by the formation of a degradation

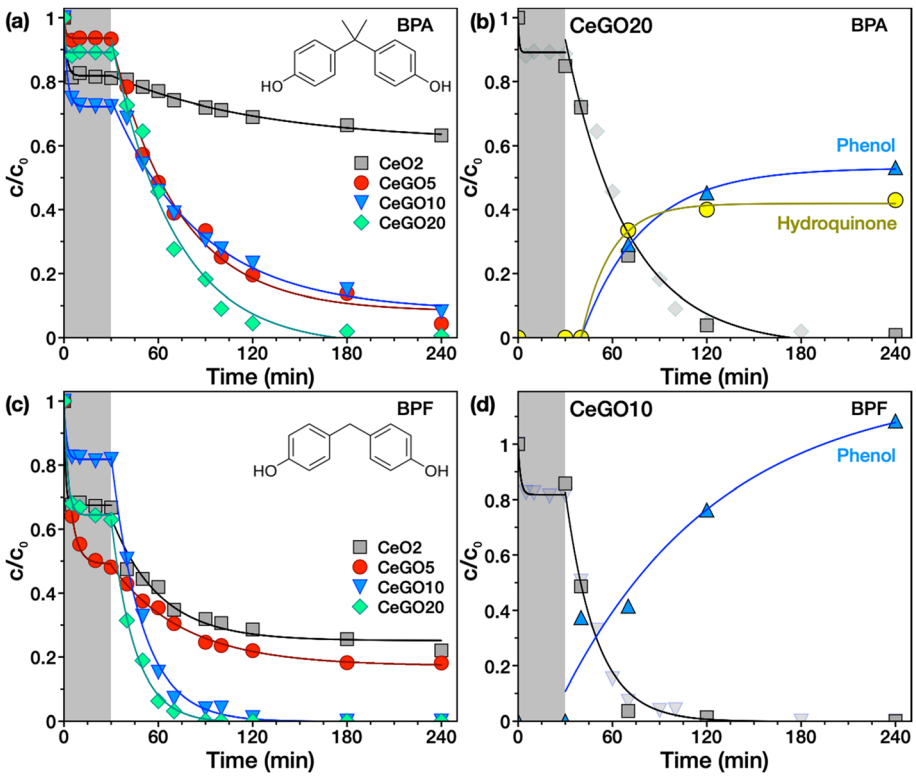

Fig. 7 Kinetics of the photocatalytic decomposition of (a) BPA and (c) BPF on ceria and CeGO composites; (b) kinetics of decomposition of BPA and product formation with the CeGO20 sample and (d) kinetics of decomposition of BPF and product formation with the CeGO10 sample as obtained by HPLC-HRMS analysis of the extracted samples. The shadow points in Fig. 7b and d show the first run of the degradation test analyzed by HPLC-DAD.

product that has a high affinity to the surface of the composite, and its accumulation thus becomes a bottleneck of the entire degradation reaction.

Analysis of the degradation products by HPLC-HRMS

To confirm that it is really a photocatalytic decomposition and describe the possible degradation mechanism, selected tests were repeated with the analysis of selected extracted time-resolved samples using HPLC-HRMS. The representative time-resolved chromatograms of BPA photodegradation using CeGO20 (see Fig. S7†) showed a rapid decrease of BPA (peak with retention time t_R ~ 6.8 min) and the formation of two possible degradation products (t_R ~ 2.8 min and t_R ~ 4.6 min), proving the effective solar-induced photodegradation of BPA on CeGO composites. Based on previous studies,[56,57] phenol and hydroquinone were suggested as possible photodegradation products, which was confirmed by comparing the retention times of unknown peaks with standards (Fig. S8†) and HRMS analysis (Fig. S9†). As evidence, the peak at t_R ~ 2.8 min corresponds to hydroquinone while the retention time of the second unknown peak (t_R ~ 4.6 min) is identical to t_R of phenol. Mass spectra of the analyzed products (Fig. S9†) show prominent peaks with a mass-to-charge ratio (m/z) of 108.0218 and 93.0347 that correspond to deprotonated molecular ions $[M - H]^-$ with a molecular mass of 109 Da and 94 Da of hydroquinone and phenol, respectively.

The results suggest that the degradation can be initiated by photogenerated ·OH radicals that attack the electron-rich C3 position on the phenyl group of BPA, which is particularly susceptible to radical attack, yielding phenol as the major product.[56] Phenol can be further oxidized by ·OH radicals to hydroquinone,[57] but it can also be formed by other oxidation pathways from various intermediate species that have not been identified. Finally, the kinetics of BPA photodegradation and production of phenol and hydroquinone on the sample CeGO20 are presented in Fig. 7b.

For BPF, chromatographic analysis (Fig. S10†) showed a rapid decrease of BPF with time (peak at t_R ~ 5.9 min) accompanied by the formation of phenol, the main degradation product identified. This again shows that BPF can be easily photodegraded by simulated solar light on CeGO composites. BPF degradation is realized by cleavage of its methylene bridge by a hydroxyl radical or other oxidizing species yielding phenol as the main degradation product. Further oxidation can probably proceed *via* hydroxylation to form, for example, catechol, which can be rapidly oxidized to hydroxyquinol (benzene-1,2,4-triol). The catechol intermediate was not detected, however, the degradation product at t_R ~ 5.4 minutes with m/z of 141.0193 was identified as hydroxyquinol (as shown in Fig. S12†), corroborating the proposed degradation pathway. Note that the amount of generated phenol plotted in the kinetics of BPF degradation (Fig. 7d) is higher than one because two molecules of phenol can be obtained by cleaving one molecule of BPF. A simple proposed degradation scheme of BPA and BPF is presented in Fig. S13.†

Conclusions

CeO_2/GO nanocomposites with 5–20 wt% of GO were prepared by a simple low-temperature (<100 °C) water-based method that enabled the *in situ* growth and crystallization of ceria nanoparticles on GO sheets, providing less aggregated exposed particles and strong interfacial interaction between the individual constituents of the composites. Furthermore, it was demonstrated for the first time that ceria-based nanomaterials are able to spontaneously decompose BPS containing sulfonyl functional groups by hydrolytic cleavage without the need of light, elevated temperature, or pH adjustment. Importantly, the CeGO composites showed an increased degradation rate compared to pure nanoceria. Moreover, the efficient solar light-induced photodecomposition of BPS, BPA and BPF was achieved on CeGO composites with the identification of the major degradation products. BPF has degraded the fastest yielding phenol as the major product, followed by BPA decomposing to hydroquinone and phenol, while BPS with the formation of *p*-phenolsulfonic acid and phenol was the most resistant to the degradation. These results point to the high potential of ceria-based materials for the removal of serious water pollutants such as bisphenols. In addition, it was shown that the mechanism of formation of nanocomposites plays an important role, and to achieve interfacial interactions it is advantageous to use methods of *in situ* growth of nanoparticles on suitable counterparts, such as graphene oxide.

Data availability

The data supporting this article have been included as part of the ESI.† The Institute of Inorganic Chemistry of the Czech Academy of Sciences (IIC) uses Fair Wizard (**https://openscience.lib.cas.cz/fair-data/**) to create the data management plan. Data are stored and archived at the digital repository of IIC operated by the Institutional Data Repository of the Czech Academy of Sciences. We are willing to share research data with interested researchers. Data available to all upon request, please contact the authors of this manuscript.

Author contributions

MŠ: methodology, investigation, analysis, data processing, and visualization. DB: investigation, analysis, and data processing. JT: investigation. PB: investigation and analysis. JČ: investigation and analysis. MK: investigation, data processing, original draft writing and editing. ID: investigation and analysis. PJ: methodology, draft – review and editing. KK: methodology, investigation, analysis, visualization, draft – review and editing JH: conceptualization, methodology, investigation, analysis, original draft writing and editing, visualization, and funding.

Conflicts of interest

There are no conflicts to declare.

Acknowledgements

This work was supported by the Research Infrastructure NanoEnviCz, supported by the Ministry of Education, Youth and Sports of the Czech Republic under Project No. LM2023066.

References

1 S.-S. Chai, W.-B. Zhang, J.-L. Yang, L. Zhang, M. M. Theint, X.-L. Zhang, S.-B. Guo, X. Zhou and X.-J. Ma, *RSC Sustainability*, 2023, **1**, 38–71.
2 C. Xu and X. Qu, *NPG Asia Mater.*, 2014, **6**, e90.
3 B. Johansson, W. Luo, S. Li and R. Ahuja, *Sci. Rep.*, 2014, **4**, 6398.
4 Z. Helali, A. Jedidi, O. A. Syzgantseva, M. Calatayud and C. Minot, *Theor. Chem. Acc.*, 2017, **136**, 100.
5 T. Montini, M. Melchionna, M. Monai and P. Fornasiero, *Chem. Rev.*, 2016, **116**, 5987–6041.
6 H. Metiu, S. Chrétien, Z. Hu, B. Li and X. Sun, *J. Phys. Chem. C*, 2012, **116**, 10439–10450.
7 M. Melchionna and P. Fornasiero, *Mater. Today*, 2014, **17**, 349–357.
8 S. Seal, A. Jeyaranjan, C. J. Neal, U. Kumar, T. S. Sakthivel and D. C. Sayle, *Nanoscale*, 2020, **12**, 6879–6899.
9 C. Tang, H. Zhang and L. Dong, *Catal. Sci. Technol.*, 2016, **6**, 1248–1264.
10 E. M. Sala, N. Mazzanti, M. B. Mogensen and C. Chatzichristodoulou, *Solid State Ionics*, 2022, **375**, 115833.
11 X. Huang, K. Zhang, B. Peng, G. Wang, M. Muhler and F. Wang, *ACS Catal.*, 2021, **11**, 9618–9678.
12 R. Augustine, Y. B. Dalvi, P. Dan, N. George, D. Helle, R. Varghese, S. Thomas, P. Menu and N. Sandhyarani, *ACS Biomater. Sci. Eng.*, 2018, **4**, 4338–4353.
13 Y. Xue, F. Yang, L. Wu, D. Xia and Y. Liu, *Adv. Healthcare Mater.*, 2024, **13**, 2302858.
14 N. Alizadeh, A. Salimi, A. Salimi, A. Salimi, T. K. Sham, P. Bazylewski and G. Fanchini, *ACS Omega*, 2020, **5**, 11883–11894.
15 Z. Tian, J. Li, Z. Zhang, W. Gao, X. Zhou and Y. Qu, *Biomaterials*, 2015, **59**, 116–124.
16 V. Baldim, F. Bedioui, N. Mignet, I. Margaill and J. F. Berret, *Nanoscale*, 2018, **10**, 6971–6980.
17 M. J. Manto, P. Xie and C. Wang, *ACS Catal.*, 2017, **7**, 1931–1938.
18 P. Janoš, I. Lovászová, J. Pfeifer, J. Ederer, M. Došek, T. Loučka, J. Henych, Z. Kolská, D. Milde and T. Opletal, *Environ. Sci.: Nano*, 2016, **3**, 847–856.
19 P. Janoš, J. Henych, J. Pfeifer, N. Zemanová, V. Pilařová, D. Milde, T. Opletal, J. Tolasz, M. Malý and V. Štengl, *Environ. Sci.: Nano*, 2017, **4**, 1283–1293.
20 P. Janoš, J. Ederer, M. Došek, J. Štojdl, J. Henych, J. Tolasz, M. Kormunda and K. Mazanec, *Environ. Sci.: Nano*, 2019, **6**, 3684–3698.
21 J. Henych, M. Šťastný, J. Ederer, Z. Němečková, A. Pogorzelska, J. Tolasz, M. Kormunda, P. Ryšánek, B. Bażanów, D. Stygar, K. Mazanec and P. Janoš, *Environ. Sci.: Nano*, 2022, **9**, 3485–3501.
22 E. T. Anthony, M. O. Ojemaye, A. I. Okoh and O. O. Okoh, *Chem. Eng. J.*, 2020, **401**, 125562.
23 K. Yu, F. Chen, L. Yue, Y. Luo, Z. Wang and B. Xing, *Environ. Sci. Technol.*, 2020, **54**, 10012–10021.
24 P. Janoš, J. Henych, O. Pelant, V. Pilařová, L. Vrtoch, M. Kormunda, K. Mazanec and V. Štengl, *J. Hazard. Mater.*, 2016, **304**, 259–268.
25 A. A. Vernekar, T. Das and G. Mugesh, *Angew. Chem., Int. Ed.*, 2016, **55**, 1412–1416.
26 A. Blum, M. Behl, L. S. Birnbaum, M. L. Diamond, A. Phillips, V. Singla, N. S. Sipes, H. M. Stapleton and M. Venier, *Environ. Sci. Technol. Lett.*, 2019, **6**, 638–649.
27 G. L. Wei, D. Q. Li, M. N. Zhuo, Y. S. Liao, Z. Y. Xie, T. L. Guo, J. J. Li, S. Y. Zhang and Z. Q. Liang, *Environ. Pollut.*, 2015, **196**, 29–46.
28 Z. Su, J. D. Hostert and J. N. Renner, *ACS ES&T Water*, 2021, **1**, 58–67.
29 S. Bhasker-Ranganath and Y. Xu, *ACS Catal.*, 2022, **12**, 10222–10234.
30 J. Henych, M. Šťastný, S. Kříženecká, J. Čundrle, J. Tolasz, T. Dušková, M. Kormunda, J. Ederer, Š. Stehlík, P. Ryšánek, V. Neubertová and P. Janoš, *Inorg. Chem.*, 2024, **63**, 2298–2309.
31 M. Zhang, S. Zhang, Z. Qi, M. Xie and Y. Qu, *Catal. Sci. Technol.*, 2024, **14**, 225–240.
32 S. Siddiqui and Z. N. Siddiqui, *Nanoscale Adv.*, 2020, **2**, 4639–4651.
33 R. Bhargava, J. Shah, S. Khan and R. K. Kotnala, *Energy Fuels*, 2020, **34**, 13067–13078.
34 R. Verma and S. K. Samdarshi, *J. Phys. Chem. C*, 2016, **120**, 22281–22290.
35 L. Xu, W.-Q. Huang, L.-L. Wang and G.-F. Huang, *ACS Appl. Mater. Interfaces*, 2014, **6**, 20350–20357.
36 J. Henych, V. Štengl, A. Mattsson, J. Tolasz and L. Österlund, *J. Hazard. Mater.*, 2018, **359**, 482–490.
37 H.-H. Huang, K. K. H. De Silva, G. R. A. Kumara and M. Yoshimura, *Sci. Rep.*, 2018, **8**, 6849.
38 S. Kumar, A. K. Ojha, D. Patrice, B. S. Yadav and A. Materny, *Phys. Chem. Chem. Phys.*, 2016, **18**, 11157–11167.
39 Fauzia, M. A. Khan, M. Chaman and A. Azam, *Sci. Rep.*, 2024, **14**, 6606.
40 W. Chen, Y.-X. Huang, D.-B. Li, H.-Q. Yu and L. Yan, *RSC Adv.*, 2014, **4**, 21619–21624.
41 B. Choudhury and A. Choudhury, *Mater. Chem. Phys.*, 2012, **131**, 666–671.
42 M. A. Gomez-Alvarez, C. Morales, J. Méndez, A. del Campo, F. J. Urbanos, A. Díaz, L. Reséndiz, J. I. Flege, D. Granados and L. Soriano, *C*, 2020, **6**, 41.
43 C. Schilling, A. Hofmann, C. Hess and M. V. Ganduglia-Pirovano, *J. Phys. Chem. C*, 2017, **121**, 20834–20849.
44 S. Claramunt, A. Varea, D. López-Díaz, M. M. Velázquez, A. Cornet and A. Cirera, *J. Phys. Chem. C*, 2015, **119**, 10123–10129.
45 A. Radoń, P. Włodarczyk and D. Łukowiec, *Phys. E*, 2018, **99**, 82–90.
46 W. Liu and G. Speranza, *ACS Omega*, 2021, **6**, 6195–6205.

47 V. Brusko, A. Khannanov, A. Rakhmatullin and A. M. Dimiev, *Carbon*, 2024, **229**, 119507.
48 M. Acik, G. Lee, C. Mattevi, M. Chhowalla, K. Cho and Y. J. Chabal, *Nat. Mater.*, 2010, **9**, 840–845.
49 H.-L. Guo, X.-F. Wang, Q.-Y. Qian, F.-B. Wang and X.-H. Xia, *ACS Nano*, 2009, **3**, 2653–2659.
50 G. N. Vayssilov, M. Mihaylov, P. St. Petkov, K. I. Hadjiivanov and K. M. Neyman, *J. Phys. Chem. C*, 2011, **115**, 23435–23454.
51 M. K. Rabchinskii, V. V. Shnitov, A. T. Dideikin, A. E. Aleksenskii, S. P. Vul, M. V. Baidakova, I. I. Pronin, D. A. Kirilenko, P. N. Brunkov, J. Weise and S. L. Molodtsov, *J. Phys. Chem. C*, 2016, **120**, 28261–28269.
52 C.-T. Chien, S.-S. Li, W.-J. Lai, Y.-C. Yeh, H.-A. Chen, I.-S. Chen, L.-C. Chen, K.-H. Chen, T. Nemoto, S. Isoda, M. Chen, T. Fujita, G. Eda, H. Yamaguchi, M. Chhowalla and C.-W. Chen, *Angew. Chem., Int. Ed.*, 2012, **51**, 6662–6666.
53 M. Zhang, S. Zhang, Z. Qi, M. Xie and Y. Qu, *Catal. Sci. Technol.*, 2024, **14**, 225–240.
54 I. El Saliby, M. Shahid, A. McDonagh, H. K. Shon and J.-H. Kim, *J. Ind. Eng. Chem.*, 2012, **18**, 1774–1780.
55 R. Mu, A. Dahal, Z.-T. Wang, Z. Dohnálek, G. A. Kimmel, N. G. Petrik and I. Lyubinetsky, *J. Phys. Chem. Lett.*, 2017, **8**, 4565–4572.
56 O. Bechambi, L. Jlaiel, W. Najjar and S. Sayadi, *Mater. Chem. Phys.*, 2016, **173**, 95–105.
57 K. Lv, X. Guo, X. Wu, Q. Li, W. Ho, M. Li, H. Ye and D. Du, *Appl. Catal., B*, 2016, **199**, 405–411.